JOURNAL OF COMPUTATIONAL PHYSICS 66, 173–196 (1986)

Computation of Turbulent Supersonic Flows around Pointed Bodies Having Crossflow Separation

DAVID DEGANI* AND LEWIS B. SCHIFF†

NASA Ames Research Center, Moffett Field, California 94035

Received September 7, 1984; revised January 22, 1986

A recently reported thin-layer parabolized Navier-Stokes method has been used to compute turbulent supersonic flows around pointed bodies at large incidence. These flow fields are complex and contain extensive regions of crossflow separation. Extensive investigations were carried out to assess the effects of grid resolution in the viscous region and inviscid region of the leeward side vortices, and the effects of the algebraic eddy-viscosity turbulence model. Comparisons between computed and experimentally measured flow fields of several pointed bodies show significant improvement in the computed flow fields obtained using a properly modified turbulence model in the crossflow separation region and adequate spatial grid resolution. The effect of adding the circumferential and cross viscous terms was found to be insignificant for the present cases. © 1986 Academic Press, Inc.

I. INTRODUCTION

The development of methods for computing flow fields surrounding bodies at large angles of attack is a topic of high current interest. This results from the requirements in modern aircraft and missile performance for higher maneuverability, and thus a trend toward flight at high angles of attack. Many current design problems, including the prediction of missile fin loads, the optimization of fighter-type aircraft engine inlets, and the heat-shield design of maneuvering reentry vehicles require detailed knowledge of high-angle-of-attack flow fields. These flow fields are complex, and typically contain extensive regions of three-dimensional crossflow separation. Crossflow separation occurs when fluid flowing circumferentially from the windward to the leeward side of the body separates from the sides of the body along a separation line nominally parallel to the longitudinal axis of the body. The fluid then rolls up to form a well defined vortex structure on the leeward side of the body. The extent of the crossflow separation and the resulting strength of the leeward-side vortex structure is typically small at low angles of attack, and grows as the angle of attack is increased. The need to

* Faculty of Mechanical Engineering, Technion–Israel Institute of Technology, Haifa, Israel.
† Research Scientist, Applied Computational Fluids Branch.

0021-9991/86 $3.00
Copyright © 1986 by Academic Press, Inc.
All rights of reproduction in any form reserved.

properly determine the crossflow separation line and the behavior of the leeward-side vortex structure makes computation of high-angle-of-attack flows difficult.

Recently [1], a numerical method based on the thin-layer form of the parabolized Navier–Stokes equations [2] was used to compute supersonic turbulent flow fields surrounding ogive–cylinder and ogive–cylinder-boattail bodies at low and moderate angles of attack ($|\alpha| \leqslant 10°$). Extensive comparisons indicated that the computed results were generally in good agreement with experimental measurements [3–5]. However, discrepancies between the computed and experimental results were seen in the regions of experimentally observed crossflow separation. The authors of [1] suggested as possible sources of these discrepancies between the computed and experimental results the lack of circumferential viscous terms within the thin-layer viscous model, and, more likely, inadequacies of the algebraic eddy-viscosity model to properly treat the regions of separated flow. We believe that another possible source of the discrepancies may have been the marginal computational resolution of the leeward-side vortex structures.

This paper reports the results of a study designed to extend the parabolized Navier–Stokes technique to treat flows over bodies at large incidence. The above-mentioned sources of discrepancy were investigated. It was found that, given a computational grid which provides adequate spatial resolution of the leeward-side vortices, a rational modification of the eddy-viscosity turbulence model that is consistent with the physics of the flows extends the applicability of the method to flows having large regions of crossflow separation. The turbulence model, once modified, was used without further changes to compute the flows around a ogive-cylinder body and several cones at various angles of attack. The computed results are in uniformly good agreement with experimental measurements throughout the flow field, for all cases considered.

In Section II we review the governing gas-dynamic equations and the numerical algorithm to illustrate the addition of circumferential viscous terms and cross terms to the thin-layer viscous model. In Section III we discuss the modifications to the turbulence model, while in Section IV we present sample results which demonstrate the accuracy and versatility of the modified numerical method.

II. Governing Equations and Numerical Scheme

Governing Gas-Dynamic Equations

The steady, three-dimensional Navier–Stokes equations, written in strong conservation-law form for Cartesian coordinates can be expressed in nondimensional variables as

$$\frac{\partial \bar{E}}{\partial x}+\frac{\partial \bar{F}}{\partial y}+\frac{\partial \bar{G}}{\partial z}=\frac{1}{\hat{R}e}\left(\frac{\partial \bar{Q}}{\partial x}+\frac{\partial \bar{R}}{\partial y}+\frac{\partial \bar{S}}{\partial z}\right). \tag{1}$$

The inviscid flux vectors in Eq. (1) are

$$\bar{E}=\bar{E}(\bar{q})=\begin{bmatrix}\rho u\\ \rho u^2+p\\ \rho uv\\ \rho uw\\ (e+p)\,u\end{bmatrix},\qquad \bar{F}=\bar{F}(\bar{q})=\begin{bmatrix}\rho v\\ \rho uv\\ \rho v^2+p\\ \rho vw\\ (e+p)\,v\end{bmatrix},$$

$$\bar{G}=\bar{G}(\bar{q})=\begin{bmatrix}\rho w\\ \rho uw\\ \rho vw\\ \rho w^2+p\\ (e+p)\,w\end{bmatrix},\qquad \bar{q}=\begin{bmatrix}\rho\\ \rho u\\ \rho v\\ \rho w\\ e\end{bmatrix}. \tag{2}$$

The internal energy of the gas is defined in terms of the conservative variables as

$$e_i=(e/\rho)-0.5(u^2+v^2+w^2) \tag{3}$$

while the equation of state for a perfect gas with ratio of specific heats γ is

$$p/\rho=(\gamma-1)\,e_i=a^2/\gamma. \tag{4}$$

The viscous flux terms in Eq. (1) are

$$\bar{Q}=\bar{Q}(\bar{q})=\begin{bmatrix}0\\ \tau_{xx}\\ \tau_{xy}\\ \tau_{xz}\\ Q_5\end{bmatrix},\qquad \bar{R}=\bar{R}(\bar{q})=\begin{bmatrix}0\\ \tau_{yx}\\ \tau_{yy}\\ \tau_{yz}\\ R_5\end{bmatrix},\qquad \bar{S}=\bar{S}(\bar{q})=\begin{bmatrix}0\\ \tau_{zx}\\ \tau_{zy}\\ \tau_{zz}\\ S_5\end{bmatrix}, \tag{5}$$

where

$$\begin{aligned}
\tau_{xx}&=\tfrac{4}{3}\mu u_x-\tfrac{2}{3}\mu(v_y+w_z),\\
\tau_{xy}&=\tau_{yx}=\mu(u_y+v_x),\\
\tau_{xz}&=\tau_{zx}=\mu(u_z+w_x),\\
\tau_{yy}&=\tfrac{4}{3}\mu v_y-\tfrac{2}{3}\mu(u_x+w_z),\\
\tau_{zz}&=\tfrac{4}{3}\mu w_z-\tfrac{2}{3}\mu(u_x+v_y),\\
Q_5&=\kappa Pr^{-1}(\gamma-1)^{-1}(a^2)_x+u\tau_{xx}+v\tau_{xy}+w\tau_{xz},\\
R_5&=\kappa Pr^{-1}(\gamma-1)^{-1}(a^2)_y+u\tau_{yx}+v\tau_{yy}+w\tau_{yz},\\
S_5&=\kappa Pr^{-1}(\gamma-1)^{-1}(a^2)_z+u\tau_{zx}+v\tau_{zy}+w\tau_{zz}.
\end{aligned} \tag{6}$$

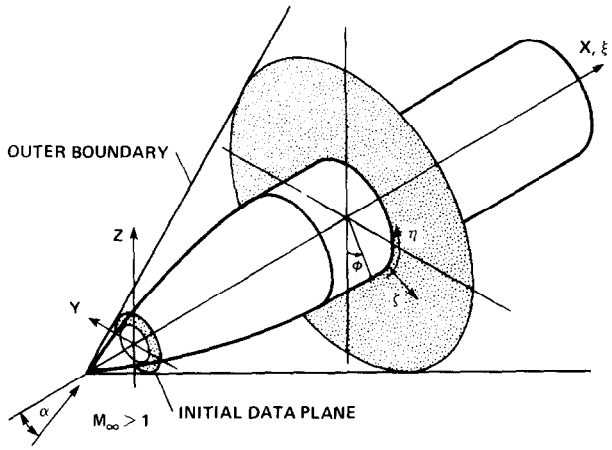

FIG. 1. Coordinates and notation.

In obtaining Eq. (6) the Stokes hypothesis was used: $\lambda = -2\mu/3$. In Eqs. (1)–(6) the Cartesian velocity components u, v, w are made nondimensional with respect to a_∞ (the freestream speed of sound), density ρ is normalized by ρ_∞ and total energy e is referenced to $\rho_\infty a_\infty{}^2$.

We introduce generalized independent spatial variables that map the physical x, y, z space surrounding a body into a rectangular ξ, η, ζ computational region. The transformation, of the form

$$\begin{aligned} \xi &= \xi(x) = \quad \text{streamwise (marching) coordinate,} \\ \eta &= \eta(x, y, z) = \text{spanwise or circumferential coordinate,} \\ \zeta &= \zeta(x, y, z) = \text{normal coordinate,} \end{aligned} \tag{7}$$

maps the body surface into the $\zeta = 0$ plane (Fig. 1). Subject to the transformation, Eq. (1) can still be expressed in strong conservation-law form as

$$\frac{\partial \hat{E}}{\partial \xi} + \frac{\partial \hat{F}}{\partial \eta} + \frac{\partial \hat{G}}{\partial \zeta} = \frac{1}{\hat{Re}}\left(\frac{\partial \hat{Q}}{\partial \xi} + \frac{\partial \hat{R}}{\partial \eta} + \frac{\partial \hat{S}}{\partial \zeta}\right), \tag{8}$$

where

$$\begin{aligned} \hat{E} &= \xi_x \bar{E}/J, \\ \hat{F} &= (\eta_x \bar{E} + \eta_y \bar{F} + \eta_z \bar{G})/J, \\ \hat{G} &= (\zeta_x \bar{E} + \zeta_y \bar{F} + \zeta_z \bar{G})/J, \end{aligned} \tag{9}$$

and

$$\hat{Q} = \hat{Q}^{\xi}(\bar{q}, \bar{q}_{\xi}) + \hat{Q}^{\eta}(\bar{q}, \bar{q}_{\eta}) + \hat{Q}^{\zeta}(\bar{q}, \bar{q}_{\zeta}) = \xi_x \hat{Q}/J, \tag{10}$$

$$\hat{R} = \hat{R}^{\xi}(\bar{q}, \bar{q}_{\xi}) + \hat{R}^{\eta}(\bar{q}, \bar{q}_{\eta}) + \hat{R}^{\zeta}(\bar{q}, \bar{q}_{\zeta}) = (\eta_x \bar{Q} + \eta_y \bar{R} + \eta_z \bar{S})/J, \tag{11}$$

$$\hat{S} = \hat{S}^{\xi}(\bar{q}, \bar{q}_{\xi}) + \hat{S}^{\eta}(\bar{q}, \bar{q}_{\eta}) + \hat{S}^{\zeta}(\bar{q}, \bar{q}_{\zeta}) = (\zeta_x \bar{Q} + \zeta_y \bar{R} + \zeta_z \bar{S})/J. \tag{12}$$

The Jacobian of the transformation, which appears in Eqs. (8)–(12), is defined as

$$J^{-1} = x_{\xi}(y_{\eta} x_{\zeta} - y_{\zeta} z_{\eta}). \tag{13}$$

The parabolized Navier–Stokes equations are obtained from Eq. (8) by neglecting all streamwise derivatives, $\partial/\partial\xi$, within the viscous terms, and by modifying the streamwise flux vector to permit stable time-like marching of the equations downstream from initial data. Following [2], we introduce the subsonic sublayer approximation, and the resulting parabolized Navier–Stokes equations can be written as

$$\frac{\partial \hat{E}_s}{\partial \xi} + \frac{\partial \hat{F}}{\partial \eta} + \frac{\partial \hat{G}}{\partial \zeta} = \frac{1}{\hat{Re}}\left[\frac{\partial}{\partial \eta}(\hat{R}^{\eta} + \hat{R}^{\zeta}) + \frac{\partial}{\partial \zeta}(\hat{S}^{\eta} + \hat{S}^{\zeta})\right]. \tag{14}$$

The modified streamwise flux vector in Eq. (14) is

$$\hat{E}_s = \left(\frac{\xi_x}{J}\right)\bar{E}_s = \left(\frac{\xi_x}{J}\right)\begin{bmatrix} \rho u \\ \rho u^2 + p_s \\ \rho uv \\ \rho uw \\ (e + p_s)\, u \end{bmatrix}, \tag{15}$$

where $p_s = p$ for supersonic flow, and p_s is defined from $\partial p/\partial \zeta = 0$ for subsonic flow in the viscous layer adjacent to the body surface. By evaluating p_s in this manner, Eq. (14) can be stably marched in the ξ direction for all flows where $u > 0$; that is, for flows without streamwise reversal (see [2] for associated stability analysis).

The viscous flux vectors in Eq. (14), $\hat{R}^{\eta}$, $\hat{R}^{\zeta}$, $\hat{S}^{\eta}$, and $\hat{S}^{\zeta}$ are given in the Appendix.

Numerical Algorithm

The numerical algorithm used to march Eq. (14) downstream is an implicit, noniterative, approximately factored finite-difference scheme, which is analogous to the one developed by Beam and Warming [6] for the solution of the unsteady Navier–Stokes equations. The marching algorithm is derived in the same manner

used by Schiff and Steger [2], but the viscous cross-derivative terms $\partial \hat{R}^{\zeta}/\partial \eta$ and $\partial \hat{S}^{\eta}/\partial \zeta$ in Eq. (14) cannot be treated implicitly, and, following Beam and Warming [6], are evaluated explicitly. The resulting algorithm can be written in so-called delta form as

$$
\begin{aligned}
&[\tilde{A}_s^j + (1-\alpha)\,\Delta\xi(\delta_\eta \tilde{B}^j - \hat{R}e^{-1}\delta_\eta \tilde{N}^j)](\tilde{A}_s^j)^{-1} \\
&\quad \times [\tilde{A}_s^j + (1-\alpha)\,\Delta\xi(\delta_\zeta \tilde{C}^j - \hat{R}e^{-1}\delta_\zeta \tilde{M}^j)]\,\Delta\hat{q}^j \\
&\quad = (\tilde{A}_s^j - \tilde{A}_s^{j-1})\,\hat{q}^j + \alpha(\hat{E}_s^j - \hat{E}_s^{j-1}) \\
&\quad\quad - (1-\alpha)\,\Delta\xi\{\delta_\eta[\eta_x^{j+1}(\bar{E}/J)^j + \eta_y^{j+1}(\bar{F}/J)^j + \eta_z^{j+1}(\bar{G}/J)^j] \\
&\quad\quad + \delta_\zeta[\zeta_x^{j+1}(\bar{E}/J)^j + \zeta_y^{j+1}(\bar{F}/J)^j + \zeta_z^{j+1}(\bar{G}/J)^j] \\
&\quad\quad - \hat{R}e^{-1}[\delta_\eta(\bar{R}^\eta)^j + \delta_\eta(\bar{R}^\zeta)^j + \delta_\zeta(\bar{S}^\eta)^j + \delta_\zeta(\bar{S}^\zeta)^j] \\
&\quad\quad - \theta\hat{R}e^{-1}[\delta_\eta(\Delta\tilde{R}^\zeta)^{j-1} + \delta_\zeta(\Delta\tilde{S}^\eta)^{j-1}]\} \\
&\quad\quad - [(\xi_x/J)^{j+1}\hat{E}_p^j - (\xi_x/J)^j\hat{E}_p^{j-1}] + D\hat{q}^j + O(\Delta\xi)^{1+3\alpha}.
\end{aligned}
\tag{16}
$$

In Eq. (16), α is set equal to 0 for first-order accuracy (Euler implicit method) and $\alpha = \frac{1}{3}$ for second-order accuracy (3-point backward differencing). Similarly, in the viscous terms $\theta = 0$ for first-order accuracy and $\theta = 1$ for second-order accuracy. The Jacobian matrices of the flux vectors, $\tilde{A}_s$, $\tilde{B}$, and $\tilde{C}$ are obtained from local linearization [7] of $\hat{E}_s$, $\hat{F}$, and $\hat{G}$. The Jacobian matrix $\tilde{M}$ is obtained from local linearization [7] of $\hat{S}^{\zeta}$ and, in an analogous manner, the Jacobian matrix $\tilde{N}$ is obtained from linearization of $\hat{R}^{\eta}$. The symbol $\tilde{}$ indicates that the matrices are evaluated using flow variables $\hat{q}$ located at $j\Delta\xi$ and metric quantities at $(j+1)\,\Delta\xi$. The term $D\hat{q}^j$ is a fourth-order explicit dissipation term, defined as

$$
D\hat{q}^j = \varepsilon_e \tilde{A}_{s\,k,l}^j \left(\frac{1}{J}\right)^j [(\nabla_\eta \Delta_\eta)^2 (J\hat{q})^j + (\nabla_\zeta \Delta_\zeta)^2 (J\hat{q})^j] \tag{17}
$$

which is added to the algorithm to suppress high-frequency oscillations. Linear stability analysis indicates that ε_e in Eq. (17) must be less than $\frac{1}{16}$ to ensure stability of the algorithm. Although adding implicit smoothing terms within the operators on the left-hand side of Eq. (16) overcomes the linear stability limit and permits the use of larger values of ε_e, no such implicit smoothing was used. While the use of implicit smoothing tends to stabilize the numerical method, the added smoothing terms can be larger than the viscous terms of interest, and thus can degrade the accuracy of the solution.

Equation (16) contains all viscous terms and viscous cross terms applicable to the parabolized Navier–Stokes equations. The thin-layer viscous model form of the equations, previously used by Schiff and Steger [2] can be obtained by neglecting all viscous terms except those solely in the normal ζ direction. Thus, by dropping the terms $\tilde{N}$, $\tilde{R}$, $\tilde{S}^{\eta}$, $\Delta\tilde{R}^{\zeta}$, and $\Delta\tilde{S}^{\eta}$ from Eq. (16), the thin-layer algorithm can be obtained.

Boundary Conditions

A computational region is established around the body, extending from the body surface to an outer boundary located outside the bow shock wave, and extending circumferentially completely around the body (Fig. 1). Implicit boundary conditions are applied at the edges of the computational grid. An implicit, no-slip, adiabatic-wall boundary condition is applied at the body surface, while free-stream conditions are maintained at the outer edge of the computational domain. A periodic continuation condition is applied at the circumferential junction of the computational region. Full details of the parabolized Navier–Stokes assumption, the derivation of the thin-layer algorithm, and the application of boundary conditions are found in [7].

Conical Solutions

In general, the initial data for the marching method must be supplied from an auxiliary computation. However, when treating the flow over conical or pointed bodies this is not necessary. As outlined in [2], for inviscid flows about conical bodies a conical grid is selected and the flow variables are initially set to free-stream values. The solution is marched one step downstream from an initial station, and the resulting flow variables are then scaled to place the solution back at the original station. The process is repeated until no change in the variables is observed with further marching. The flow variables are then constant along rays of the flow field, and a conical solution has been generated. Upon assuming flow variables within the viscous layer to also be constant along rays, the same procedure can be used to generate viscous conical solutions. Although viscous flow cannot be strictly conical, the assumption that the flow variables are locally conical along rays is reasonable when treating high-Reynolds-number flows. The validity of the assumption of locally conical viscous flows has been demonstrated in [1]. The marching-stepback procedure was utilized to generate the conical solutions in the present work.

III. Turbulence Model

The coefficients of viscosity and thermal conductivity contained in the viscous terms of Eq. (16) are specified using an algebraic eddy-viscosity turbulence model. In this section we discuss the physical justification for applying simple eddy-viscosity models to complex flows having regions of crossflow separation, review the details of the model, and discuss its implementation, within the code, for the region of crossflow separation.

Physical Justification

Eddy-viscosity turbulence models such as the one described below are usually derived and validated for two-dimensional boundary-layer flows. Further, the eddy-viscosity coefficient determined by these models depends only on the local normal

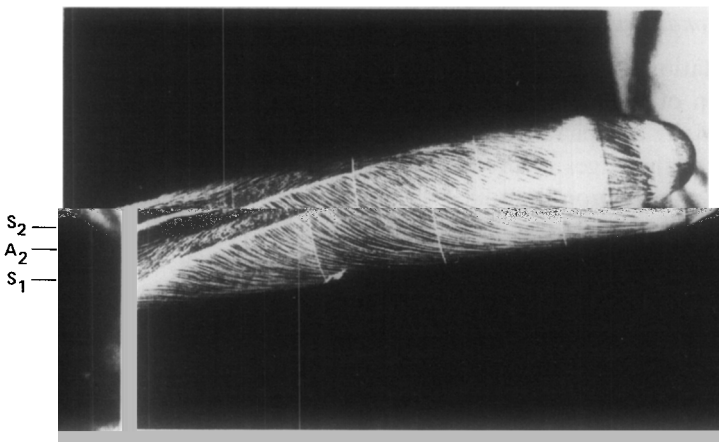

FIG. 2. Surface oil-flow patterns on 20° half-angle blunted cone-cylinder at $M_\infty = 2.3$, $\alpha = 12°$, $Re_L \approx 10 \times 10^6$, $L = 15$ in.

flow profiles. The justification for applying such models to three-dimensional flows having crossflow separation can be seen if we examine the structure of such flows. A typical flow over an inclined body of revolution is seen in Fig. 2, which shows experimental surface skin-friction lines obtained by Boersen [8] on a blunted cone-cylinder body at $\alpha = 12°$ using an oil-flow technique. At this angle of attack no crossflow separation is observed near the nose of the body. Crossflow separation is observed to start approximately three body diameters downstream from the nose, $x/d \approx 3$, as evidenced by the convergence of skin friction lines toward the primary separation line, located at S_1. This is so-called local separation (see [9] for further discussion). A secondary separation line located at S_2 is observed to start at $x/d \approx 5$. The corresponding flow structure above the body is shown schematically in Fig. 3 for a crossflow plane, i.e., a plane normal to the body axis of symmetry, downstream of the origin of the secondary separation. The outer flow approaching the windward plane of symmetry turns and flows outward along the body from the windward toward the leeward side under the action of circumferential pressure gradients; it develops a well-defined boundary layer. The boundary layer separates from the body at a primary separation point, at $\phi = \phi_{S_1}$. The fluid leaves the body along a feeding sheet and rolls up to form a primary vortex structure on the leeward side of the body. The strength of the primary vortices grows with increased distance downstream in an analogous manner to the growth, with time, of the vortices behind a two-dimensional cylinder in crossflow impulsively started from rest. The primary vortices induce a downflow, i.e., a flow toward the body surface, on the leeward plane of symmetry. The induced downflow turns outward along the body surface from the point of attachment at the leeward plane of symmetry and flows toward the windward side. If the primary vortex strength is sufficiently large, the adverse circumferential pressure gradient outboard of the vortices causes the induced flow to separate at a secondary separation point, at $\phi = \phi_{S_2}$. This fluid rolls

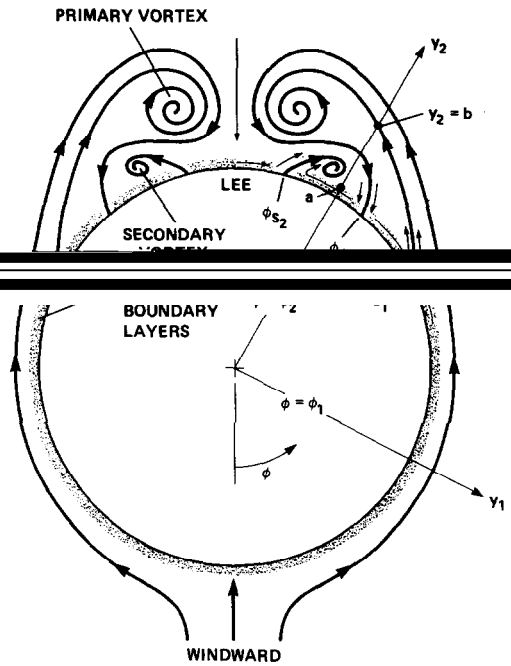

FIG. 3. Flow structure in the crossflow plane.

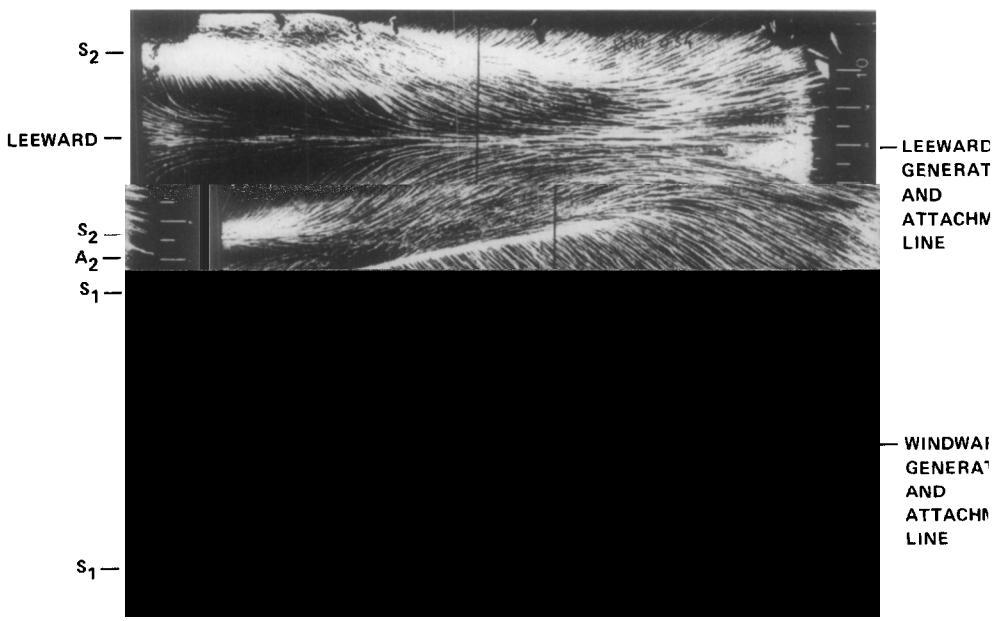

FIG. 4. Unwrapped surface oil-flow patterns on cylindrical afterbody of blunted cone-cylinder fro
Fig. 2.

up behind the body to form the secondary vortex structure. Another point of attachment is located on the body surface between the primary and secondary separation points, at $\phi = \phi_A$. As shown in Fig. 3, fluid flows downward toward the attachment point and outward along the body surface from the attachment point toward the crossflow separation points.

In addition to the crossflow velocity shown in Fig. 3, an axial component carries the flow downstream. The combined action of the circumferential and axial components at the body surface may be seen in Fig. 4, which shows the surface skin-friction lines on the unwrapped cylindrical afterbody of the body shown in Fig. 2. The convergence of surface skin-friction lines toward the primary and secondary separation lines and the circumferential divergence of the skin-friction lines from the attachment line at A, $(\phi = \phi_A)$ and at the leeward symmetry plane are clearly visible. Thus, the flow is observed to consist of a series of attached boundary layers underlying the leeward-side vortex structure. The vortex structure itself is essentially inviscid, and is governed primarily by the convection of vorticity generated within the boundary layers at the body surface. Since the primary direction of these boundary layers is streamwise, they should all be turbulent under those conditions where the windward-side flow is turbulent. Thus, the application of an eddy-viscosity model, which depends only on the local flow profiles, is justified within the attached boundary layers underlying the leeward-side vortex structures, as well as within the windward-side boundary layer.

Eddy-Viscosity Model

In this discussion we adopt the dimensional notation of Baldwin and Lomax [10]. The resulting coefficients can be nondimensionalized for use in Eq. (16) by normalizing them by their free-stream (laminar) values.

For laminar flow computations the coefficient of molecular viscosity $\mu = \mu_l$ is obtained from Sutherland's law and the coefficient of thermal conductivity κ is specified, assuming a constant Prandtl number, as $\kappa_l/c_p = \mu_l/Pr$. For turbulent-flow computations the laminar-flow coefficients are replaced by

$$\begin{aligned} \mu &= \mu_l + \mu_t, \\ \frac{\kappa}{c_p} &= \frac{\mu_l}{Pr} + \frac{\mu_t}{Pr_t}. \end{aligned} \tag{18}$$

The turbulent viscosity coefficient μ_t is computed using the isotropic, two-layer, Cebeci-type, algebraic eddy-viscosity model reported by Baldwin and Lomax [10].

In the Baldwin–Lomax formulation μ_t is given by

$$\mu_t = \begin{cases} (\mu_t)_{\text{inner}}, & y \leqslant y_c \\ (\mu_t)_{\text{outer}}, & y > y_c, \end{cases} \tag{19}$$

where y is the local distance measured normal to the body surface and y_c is the

smallest value of y at which the values from the inner and outer region formulas are equal. Within the inner region

$$(\mu_t)_{\text{inner}} = \rho l^2 |\omega|, \tag{20}$$

where

$$l = ky[1 - e^{-(y^+/A^+)}]; \tag{21}$$

$|\omega|$ is the magnitude of the local vorticity vector, and

$$y^+ = (\sqrt{\rho_w \tau_w}/\mu_w)\, y \tag{22}$$

In the outer region, for attached boundary layers the turbulent viscosity coefficient is given by

$$(\mu_t)_{\text{outer}} = KC_{cp}\rho F_{\text{wake}} F_{\text{kleb}}(y) \tag{23}$$

In Eq. (23) K and C_{cp} are constants, F_{kleb} is the Klebanoff intermittency factor, and

$$F_{\text{wake}} = y_{\max} F_{\max}, \tag{24}$$

where $F_{\max}$ is the maximum value that the function $F(y)$, defined as

$$F(y) = |\omega|\, y[1 - e^{-(y^+/A^+)}] \tag{25}$$

takes in a local profile, and $y_{\max}$ is the value of y at which $F_{\max}$ occurs. The constants appearing in Eqs. (18)–(25) were determined in [10] by requiring the boundary-layer profiles computed with the model to be in agreement with those determined using the Cebeci [11] formulation. The values were determined to be

$$\begin{aligned} Pr &= 0.72, & k &= 0.4, \\ Pr_t &= 0.9, & K &= 0.0168, \\ A^+ &= 26, & C_{cp} &= 1.6. \end{aligned} \tag{26}$$

Model Implementation

The major difficulty encountered in applying the Baldwin–Lomax turbulence model to bodies with crossflow separation is that of properly evaluating the scale length $y_{\max}$ and in turn, of determining $(\mu_t)_{\text{outer}}$ for boundary-layer profiles in the crossflow separation region. This difficulty becomes apparent upon considering the behavior of the function $F(y)$ [Eq. (25)] along two rays, one located on the windward side at $\phi = \phi_1$ and the other on the leeward side at $\phi = \phi_2$ (Fig. 3). The functions are shown schematically in Figs. 5(a) and (b), respectively. On the windward side the attached boundary layer gives rise to a profile of $F(y)$ which has

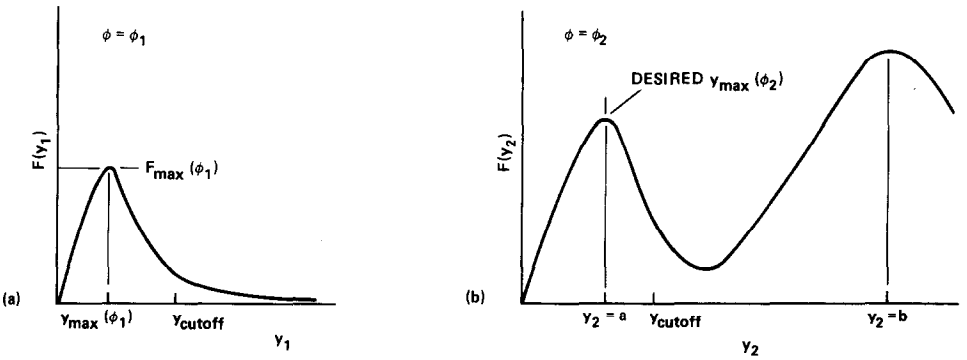

FIG. 5. Behavior of $F(y)$ at large incidence. (a) $\phi = \phi_1$ (windward side), (b) $\phi = \phi_2$ (leeward side).

a single, well-defined, peak, as shown in Fig. 5(a). Thus, the determination of $F_{max}(\phi_1)$, $y_{max}(\phi_1)$, and $F_{wake}(\phi_1)$ is straightforward. However, on the leeward-side ray [Fig. 5(b)], in addition to a local peak in $F(y)$ in the attached boundary layer at $y_2 = a$, the overlying vortex structure causes a larger peak in $F(y)$ at $y_2 = b$. As originally implemented, the computer code searches outward along each ray to determine the maximum in $F(y)$, and would, in this instance, select the peak in $F(y_2)$ occurring at $y_2 = b$. The choice of the peak at $y_2 = b$ results in a value of $F_{wake}(\phi_2)$ and, in turn, a value of the outer layer eddy-viscosity coefficient $(\mu_t)_{outer}$ which is much too high. The resulting value is at least one order of magnitude larger and can be as much as two orders of magnitude larger than the value of $(\mu_t)_{outer}$ resulting from evaluating $F_{wake}(\phi_2)$ from the peak at $y_2 = a$. Thus, in general, the computed eddy-viscosity coefficient in the crossflow separation region behind the primary separation point will be too high. This will cause the details of the computed flow to be distorted or washed out. In particular, the primary vortices will be smaller than those observed experimentally and the primary separation point will be located closer to the leeward symmetry plane. In addition, the secondary separation and secondary vortices will not appear in the computed flow.

To eliminate these difficulties we have modified our implementation of the turbulence model. At each axial station the code searches radially outward along successive rays, sweeping from the windward to the leeward plane of symmetry. Along each ray the code sweeps outward to find the first peak in $F(y)$, and cuts off the search when the peak is reached. To prevent the selection of extraneous peaks which might be caused by a nonsmooth behavior in $F(y)$, a peak is considered to have been found when the value of $F(y)$ drops to 90% of the local maximum value. Choice of F_{max} in this manner will exclude the second, spurious, maximum [see Fig. 5(b)].

For most rays in the crossflow separation region the two peaks in $F(y)$ are spaced far enough apart that the logic described above will select the first peak. However, this is not true for rays in the vicinity of the primary separation point (and to a lesser extent for rays in the immediate vicinity of the secondary separation

point). Along these rays the vortex feeding sheets lie close to the outer edge of the attached boundary layers: the peaks in $F(y)$ merge. Under these conditions the code would choose a value of y_{max} near the top edge of the feeding sheet. Consequently, a further test is applied. On each ray (except the ray on the windward plane of symmetry) a cutoff distance is specified in terms of y_{max} from the previous ray, i.e., $y_{cutoff}(\phi) = cy_{max}(\phi - \Delta\phi)$, where c is a constant chosen equal to 1.5. If no peak in $F(y)$ is found along a ray for $y \leqslant y_{cutoff}$ the values of F_{max} and y_{max} are taken as those found on the previous ray. In this manner a physically reasonable value of the eddy-viscosity coefficient will be chosen for those rays close to the crossflow separation points.

It is readily apparent that conditions within the boundary layers which leave the body at the primary separation points are related to the conditions within the boundary layers on the windward side of the body. Further, it is physically reasonable to expect that the boundary-layer quantities vary smoothly circumferentially around the body. Thus, specifying the cutoff distance in terms of the values on the previous ray, and taking the values of y_{max} and F_{max} from those of the adjacent ray, allows the model to be applicable in a rational manner over a wide range of local flow conditions, and in particular, for varying local Reynolds numbers.

The various coefficients appearing in the Baldwin–Lomax turbulence model were varied to assess their effect on the computed boundary-layer profiles. The best match with experimental measurements was obtained with the coefficients set at the values suggested in Eq. (26).

IV. Results

An extensive series of computations has been carried out to assess the accuracy and validity of the parabolized Navier–Stokes technique and the modified turbulence model to treat flows having large crossflow separation. Cases treated include three cones of various half angles and angles of attack for which experimental high-angle-of-attack flow-field data is available. In addition, computations were carried out for the ogive-cylinder body previously considered in [1]. The results presented here are condensed from a large number of numerical computations in which the grid resolution was varied. In all cases the grids consisted of 50 nonuniformly spaced points in the radial direction between the body and the outer boundary. The radial stretching was chosen to give a value of $y^+ \approx 1$ at the first point above the body on the windward plane of symmetry, where the bow shock wave and grid outer boundary lie close to the body surface. The radial spacing increased smoothly in the circumferential direction, and had a value of $y^+ \approx 5$ at the first point above the body on the leeward plane of symmetry. A grid having a y^+ less than 5 had been found necessary in [1] to give adequate resolution of the turbulent boundary layer. Computations carried out during the present study with grids having finer radial resolution in the attached boundary layers confirmed that the above grid resolution was adequate to obtain accurate turbulent-flow results.

Effect of Circumferential Viscous Terms

At each of the grid resolutions considered, computations were carried out with both the old and the modified turbulence model. Further, to assess the validity of the thin-layer viscous model for flows with crossflow separation, each computation was carried out with and without the circumferential viscous terms and viscous cross terms included in the code. The circumferential viscous terms are formally of higher order than the radial terms, and thus should have only a negligible effect. Further, practical circumferential grid resolutions are not sufficiently fine to accurately resolve these terms. However, the terms were included in the code to resolve a controversy in which several researchers have asserted that one cannot accurately compute crossflow separated flows if the cross and circumferential viscous terms are not present. As expected, addition of the circumferential viscous terms caused only very slight changes in the computed solutions (less than 0.5%), much smaller than those due to the modifications within the turbulence model. An analogous conclusion regarding the effect of the circumferential and cross viscous terms was reached by Degani and Steger [12] from computations based on the two-dimensional time-dependent form of the Navier–Stokes equations. Although inclusion of the additional viscous terms did not appear to be necessary, and despite the fact that including them increases the computation time by approximately 11%, they were retained in the code for all results shown below. In addition, with the exception of those cases for which changes to the computational method are explicitly noted, all results were obtained with a computational grid of 50 radial and 72 circumferential points, and with the modified turbulence model. Computation time for this size grid was 1.9 sec/step on a CRAY–1 computer.

Effect of Turbulence Model

Ogive-Cylinder. Computations were carried out for the flow field surrounding the 13.5-inch-long ogive-cylinder model previously considered in [1]. A sketch of the model is contained in Fig. 6. Surface-pressure measurements [3] have been obtained on this body at angles of attack ranging up to 10.4°, and boundary-layer profiles measured [4, 5] for angles of attack ranging up to 6.3°, at free-stream conditions of $M_\infty = 3.0$ and $Re_l = 7.30 \times 10^6$ based on the model length.

Ogive-Cylinder, $\alpha = 6.3°$. Circumferential surface-pressure distributions obtained using both the old and the modified turbulence model at $\alpha = 6.3°$ and at an axial station, $x = 12.99$ in., near the rear of the cylinder section, are shown in Fig. 6. As was discussed in [1], in this range of angle of attack crossflow separation does not occur on the body near the nose, but is observed to start downstream of the ogive-cylinder junction and to grow with increasing distance downstream. Further, at a fixed axial station on the cylinder, the extent of the crossflow separation grows with increasing incidence. Surface-pressure distributions computed with both models at $\alpha = 4.2°$ (not shown), where the crossflow separation is small, were identical to plotting accuracy. At $\alpha = 6.3°$ the separation region is still observed to be relatively small, even at the rear of the body, and the pressure distributions computed using

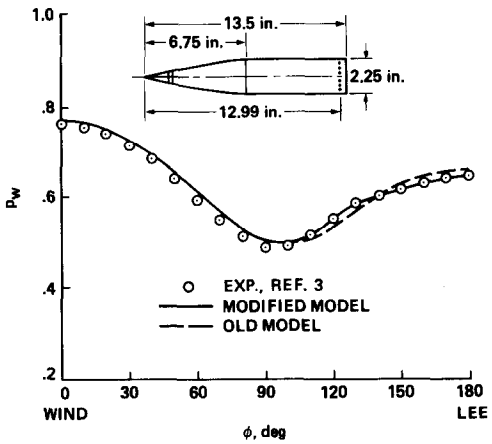

FIG. 6. Circumferential surface-pressure distributions on ogive-cylinder body; $M_\infty = 3.0$, $\alpha = 6.3°$, $x = 12.99$ in., $Re_x = 7.03 \times 10^6$.

both turbulence models are close, although the distribution computed with the modified model is in better agreement with the measured pressures.

A more sensitive test of the accuracy of the numerical method is its ability to compute the boundary-layer velocity profiles. It was found in [1] that at $\alpha = 4.2°$ a slight discrepancy was observed between velocity profiles measured at the rear of the cylinder section and those computed with the old turbulence model, for rays on the leeward side of the body. At $\alpha = 6.3°$ these discrepancies appear more pronounced. In particular, the computed profile on the leeward symmetry plane indicated a velocity deficit compared to the measured profile, while the one computed at $\phi = 150°$ showed too full a profile. The improvement in the boundary-layer profiles computed with the modified turbulence model at $\alpha = 6.3°$ is evident in Fig. 7. Profiles at $\phi = 120°$, 150°, and on the leeward symmetry plane are shown in Figs. 7(a), (b), and (c), respectively. The overprediction in computed velocity at $\phi = 150°$ is greatly reduced with the use of the modified model. In addition, the deficit in the computed velocity at $\phi = 180°$ is slightly reduced with the use of the modified model. Computations carried out at $\alpha = 4.2°$ with the modified model (not shown) demonstrate analogous improved comparison with the experimental measurements.

Ogive-Cylinder, $\alpha = 10.4°$. Circumferential surface-pressure distributions, obtained at $\alpha = 10.4°$, are shown in Fig. 8 for two axial stations; one at $x = 7.04$ in. [Fig. 8(a)] just downstream of the ogive-cylinder junction, the other at $x = 12.99$ in. [Fig. 8(b)]. Even at this higher angle of attack, at the forward station no crossflow separation was observed experimentally or in the computed results. As a result, the surface pressures computed with both turbulence models and agree well with experiment. However, experimental vapor screen photos supplied by Nietubicz [13] reveal that at the rearward station the leeward-side vortex structure is well developed. The improvement obtained in the pressure distribution on the leeward side of the body using the modified turbulence model, which takes proper

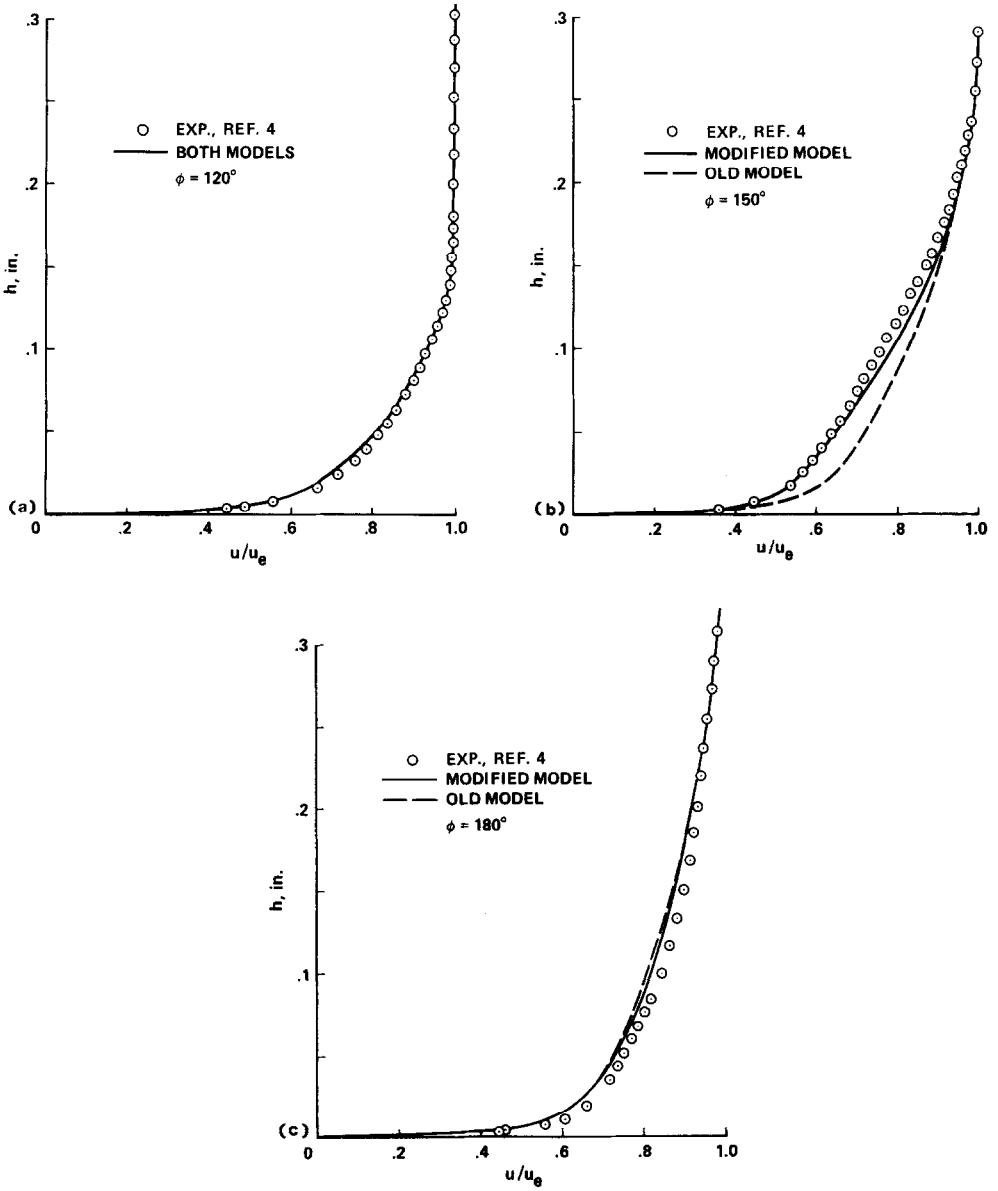

FIG. 7. Boundary-layer velocity profiles on ogive-cylinder body; $M_\infty = 3.0$, $\alpha = 6.3°$, $Re_x = 6.77 \times 10^6$. (a) $\phi = 120°$, (b) $\phi = 150°$, (c) $\phi = 180°$ (leeward ray).

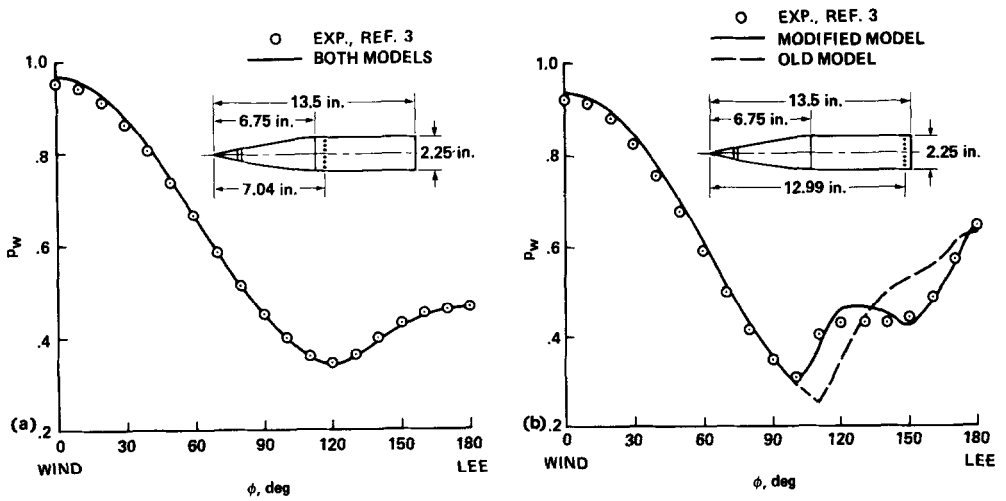

FIG. 8. Circumferential surface-pressure distributions on ogive-cylinder body; $M_\infty = 3.0$, $\alpha = 10.4°$. (a) $x = 7.04$ in., $Re_x = 3.81 \times 10^6$, (b) $x = 12.99$ in., $Re_x = 7.03 \times 10^6$.

account of the vortex structure, is striking. The extent of the computed crossflow separation region is evident from the crossflow velocity vectors shown in Fig. 9, which were computed with the modified model.

12.5° Cone. Experimental measurements have been made [14] of the flow field surrounding a 40.6 in., 12.5° half-angle cone model in the 5-ft trisonic wind tunnel of the National Aeronautical Establishment (NAE), Canada. The test conditions were $M_\infty = 1.8$ and a free-stream Reynolds number of 25×10^6 based on the model axial length. Surface-pressure distributions were obtained in addition to profiles of

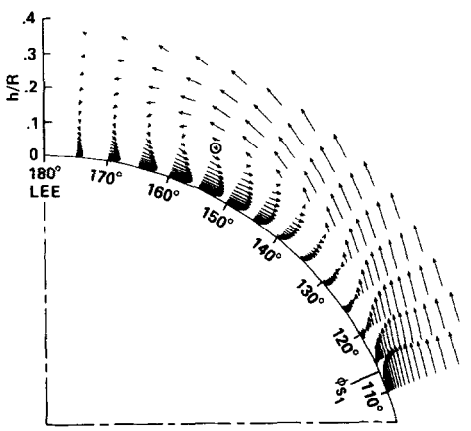

FIG. 9. Computed crossflow plane velocity vectors on ogive-cylinder body; $M_\infty = 3.0$, $\alpha = 10.4°$, $x = 12.50$ in., $Re_x = 6.77 \times 10^6$.

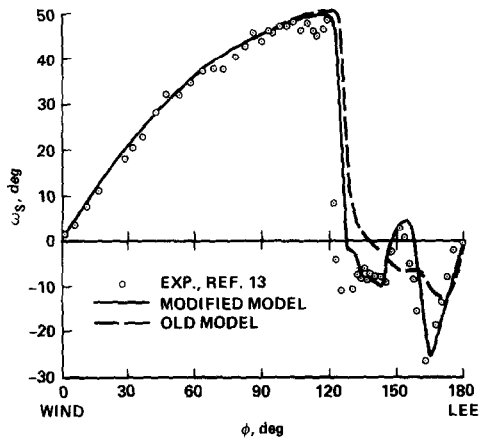

FIG. 10. Surface flow direction on 12.5° cone; $M_\infty = 1.80$, $\alpha = 22.75°$, $Re_x = 21.25 \times 10^6$.

the boundary-layer velocity and direction. Conical flow computations were carried out for corresponding conditions with the body at an angle of attack of 22.75°, a relative incidence α/θ_c of 1.82. A grid having 50 radial and 144 circumferential points was utilized.

Experimental measurements of the surface flow direction (Fig. 10) show two separation points and a reattachment point between them. However, calculations made using the old turbulence model show only one separation point, at it was located too close to the leeward symmetry plane. When the modified model was used, results similar to the experiments were obtained. To understand the origin of the differences between the results from the two models, it is helpful to examine the crossflow velocity vector plots for the leeward side of the cone. The results from the modified model (Fig. 11(a)) show a flow structure similar to that shown

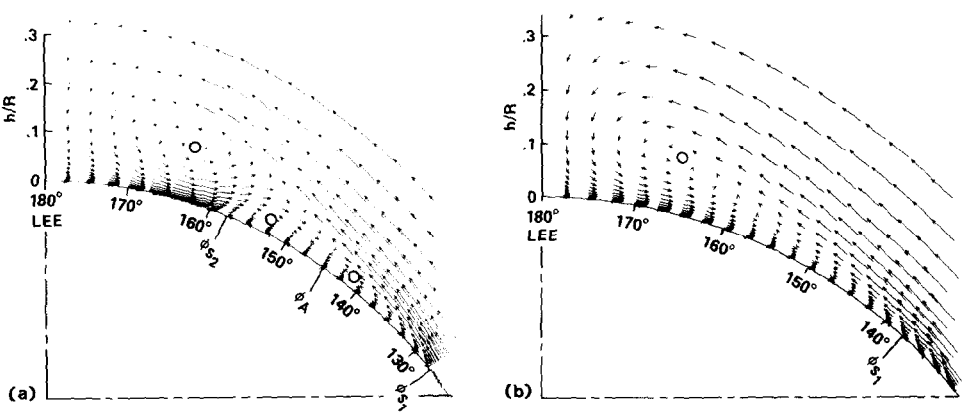

FIG. 11. Computed crossflow plane velocity vectors on 12.5° cone; $M_\infty = 1.80$, $\alpha = 22.75°$, $Re_x = 21.25 \times 10^6$. (a) Modified turbulence model, (b) old turbulence model.

schematically in Fig. 3. The primary vortex, at $\phi = 163°$, and the secondary vortex, at $\phi = 153°$, are both clearly noticeable. Their centers are indicated by the open circles. In addition, a weak tertiary vortex, having the same rotation as the primary vortex, is observed at $\phi = 142°$. Similar tertiary vortices have been observed experimentally. On the other hand, the crossflow velocity vector plot obtained using the old model (Fig. 11(b)) shows a primary vortex which is located too close to the leeward symmetry plane, at $\phi = 166°$, and lies closer to the body surface. Further, the secondary and tertiary vortices are absent. Moreover, only one separation point is seen and it is located too close to the leeward symmetry plane, while in Fig. 11(a) the separation and reattachment points are located as observed in the experiments.

5° Cone. An additional demonstration of the accuracy of the parabolized Navier–Stokes method for flows having large crossflow separation is the comparison between the measured and computed flow-field results for a 5° half-angle cone at an angle of attack of 12.5° ($\alpha/\theta_c = 2.5$). The measurements were conducted on a 54-in.-long cone model which was tested in the NAE 5-ft trisonic wind tunnel [15] at $M_\infty = 1.8$ and a free-stream Reynolds number of 34×10^6 based on the model length. Conical flow computations were carried out at these conditions using the 50 by 144 point grid and the modified turbulence model discussed above. The constants within the model are identical to those used for the 12.5° cone computations. The ability of the numerical method to determine details of the leeward-

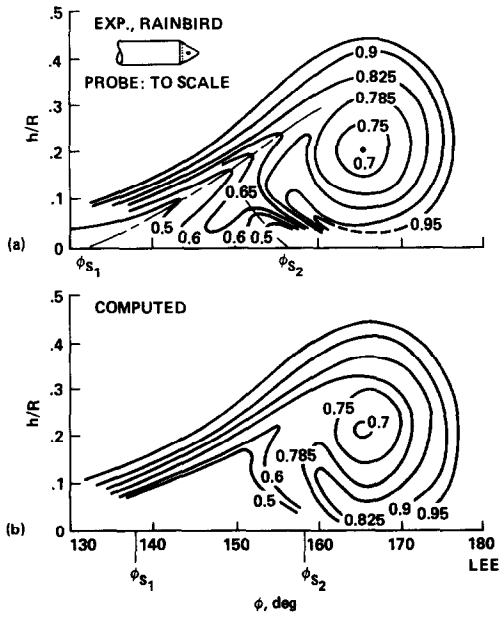

FIG. 12. Normalized pitot-pressure contours in flow field above yawed 5° cone; $M_\infty = 1.80$, $\alpha = 12.5°$, $Re_x = 28.9 \times 10^6$. (a) Experiment [15], (b) computed.

side vortex structure is shown in Fig. 12, which shows measured and computed contours of pitot pressure, normalized by free-stream pitot pressure, above the leeward side of the body in a crossflow plane. The location of the computed pressure contours surrounding the primary vortex are in remarkably close agreement with those determined from experiment.

Effects of Grid Spacing

The choice of a computational grid for any flow-field computation is dependent on the scale of the flow structures that must be resolved. For high-angle-of-attack flows, adequate resolution must be provided for the attached boundary layers as well as for the details of the leeward-side vortex structure. Insufficient resolution of the vortex structure results in poor definition of the underlying boundary-layer edge conditions, and correspondingly poor computed results, even though the modified turbulence model is employed.

The effect that circumferential grid spacing has on the resolution of the flow structures can be seen by examining the velocity vectors shown in Fig. 13, for flow over a 7.5° half-angle cone at $\alpha = 22.6°$, $\alpha/\theta_c = 3.0$, and $M_\infty = 2.94$. The velocity vectors shown in Fig. 13(a) were obtained using a circumferential grid spacing, $\Delta\phi = 2.5°$, while those shown in Fig. 13(b) were computed with a circumferentially coarser grid, $\Delta\phi = 5.0°$, and having the same radial spacing. The results obtained with the coarse grid fail to resolve the small-scale structure of the flow. In particular, the secondary separation point is located at $\phi = 155°$, as opposed to the value of $\phi = 160°$ obtained in the fine-grid results. Further, the secondary vortex structure, located at $\phi = 150°$ and the tertiary vortex, located at $\phi = 142°$ in Fig. 13(a), are not observed in the coarse-grid results.

Experiments were carried out [16, 17] at the University of Technology, Delft, The Netherlands, for this case. Contours of constant pressure measured in the flow

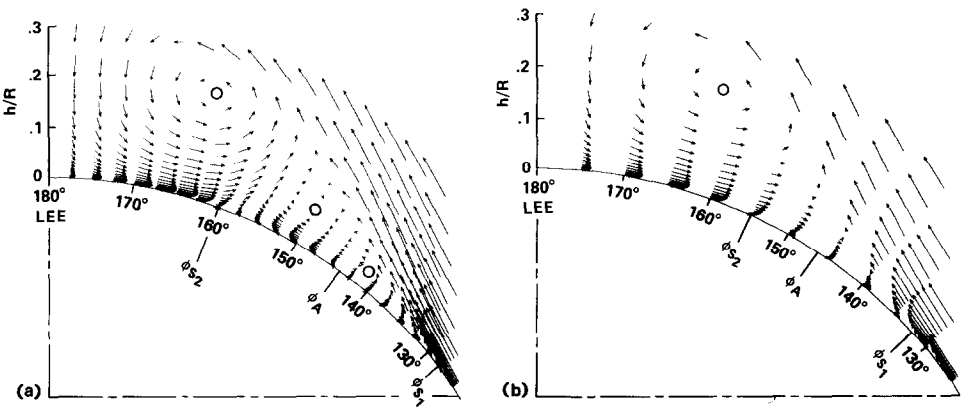

FIG. 13. Computed crossflow plane velocity vectors on 7.5° cone; $M_\infty = 2.94$, $\alpha = 22.6°$, $Re_x = 5.85 \times 10^6$. (a) $\Delta\phi = 2.5°$, (b) $\Delta\phi = 5.0°$.

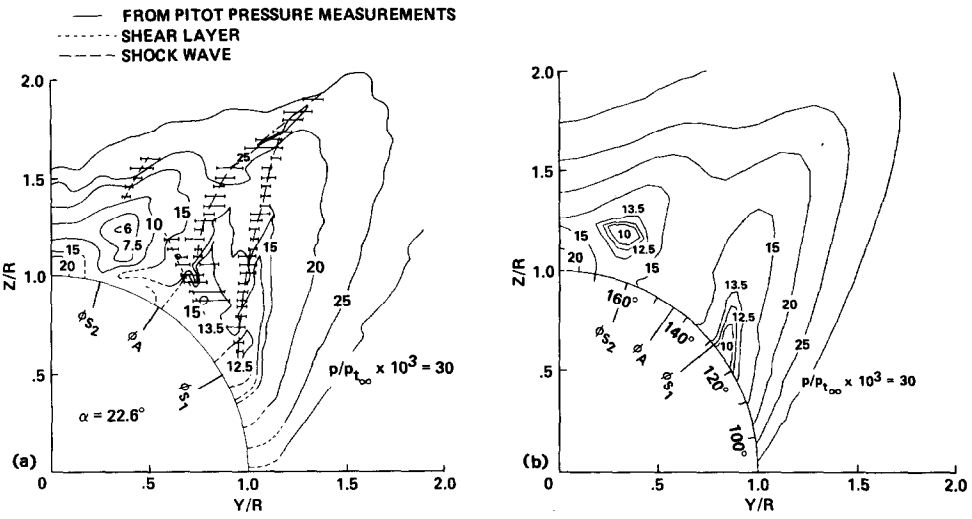

FIG. 14. Pressure contours in flow field above yawed 7.5° cone; $M_\infty = 2.94$, $\alpha = 22.6°$, $Re_x = 5.85 \times 10^6$. (a) Experiment [16], (b) computed.

field above the leeward side of the body are shown in Fig. 14(a), and the corresponding computed contours are shown in Fig. 14(b). The computed contours are in good agreement with the measured ones. In addition, the computed separation and reattachment points are in good agreement with the measured values, in contrast to these points obtained using the coarser grid (Fig. 13(b)).

As we have mentioned previously, the choice of a computational grid is governed by the scale of the flow structures that must be resolved. It appears that, for the cases considered here, a circumferential grid spacing of $\Delta\phi = 2.5°$ is necessary to give accurate results. For bodies at lower angles of attack, where the secondary vortices are less pronounced and have less effect on the flow, a grid spacing sufficient to resolve only the primary vortices may prove adequate. On the other hand, if detailed knowledge of the secondary vortex structure, or of the still smaller vortices which occur near the primary separation points, is of importance, grids having finer circumferential spacings than those used in the present work will be required.

CONCLUDING REMARKS

This paper has reported the results of a study in which the thin-layer parabolized Navier–Stokes finite-difference method developed by Schiff and Steger was modified to compute the turbulent supersonic flows surrounding pointed bodies at large angles of attack. These flow fields are characterized by crossflow separation, in

which fluid separates from the sides of the body and rolls up on the leeward side to form a well-defined vortex pattern. Proper numerical simulation of such flows was found to depend on:

(1) adequate radial resolution of the attached turbulent viscous layers,

(2) adequate radial and circumferential resolution of the leeward vortices, and

(3) a rational modification of the algebraic eddy-viscosity model employed, to permit a proper evaluation of the viscous-layer scale length under the leeward vortex structure.

The inclusion or neglect of circumferential velocity derivative terms in the viscous terms of the gas-dynamic equations was investigated, and was found to have only negligible effects for the high-Reynolds-number flows considered in this study.

Appendix

The viscous flux vectors in Eq. (14) are

$$\hat{R}^{\eta} = J^{-1}\begin{bmatrix} 0 \\ \frac{1}{3}\mu\eta_x(\eta_x u_\eta + \eta_y v_\eta + \eta_z w_\eta) + \mu(\eta_x^2+\eta_y^2+\eta_z^2)\,u_\eta \\ \frac{1}{3}\mu\eta_y(\eta_x u_\eta + \eta_y v_\eta + \eta_z w_\eta) + \mu(\eta_x^2+\eta_y^2+\eta_z^2)\,v_\eta \\ \frac{1}{3}\mu\eta_z(\eta_x u_\eta + \eta_y v_\eta + \eta_z w_\eta) + \mu(\eta_x^2+\eta_y^2+\eta_z^2)\,w_\eta \\ \{(\eta_x^2+\eta_y^2+\eta_z^2)[\mu(uu_\eta + vv_\eta + ww_\eta) + \kappa Pr^{-1}(\gamma-1)^{-1}(a^2)_\eta] \\ \quad + \frac{1}{3}\mu(\eta_x u + \eta_y v + \eta_z w)(\eta_x u_\eta + \eta_y v_\eta + \eta_z w_\eta)\} \end{bmatrix}, \tag{A1}$$

$$\begin{bmatrix} 0 \\ \mu[u_\zeta(\frac{4}{3}\eta_x\zeta_x + \eta_y\zeta_y + \eta_z\zeta_z) + v_\zeta(\eta_y\zeta_x - \frac{2}{3}\eta_x\zeta_y) + w_\zeta(\eta_z\zeta_x - \frac{2}{3}\eta_x\zeta_z)] \\ \mu[u_\zeta(\eta_x\zeta_y - \frac{2}{3}\eta_y\zeta_x) + v_\zeta(\eta_x\zeta_x + \frac{4}{3}\eta_y\zeta_y + \eta_z\zeta_z) + w_\zeta(\eta_z\zeta_y - \frac{2}{3}\eta_y\zeta_z)] \\ \mu[u_\zeta(\eta_x\zeta_z - \frac{2}{3}\eta_z\zeta_x) + v_\zeta(\eta_y\zeta_z - \frac{2}{3}\eta_z\zeta_y) + w_\zeta(\eta_z\zeta_z + \eta_x\zeta_x + \frac{4}{3}\eta_y\zeta_y)] \\ \quad + \mu v_\zeta(\frac{4}{3}v\eta_y\zeta_y + u\eta_y\zeta_x + v\eta_x\zeta_x + w\eta_y\zeta_z + v\eta_z\zeta_z - \frac{2}{3}u\eta_x\zeta_y - \frac{2}{3}w\eta_z\zeta_y) \\ \quad + \mu w_\zeta(\frac{4}{3}w\eta_z\zeta_z + u\eta_z\zeta_x + v\eta_z\zeta_y + w\eta_x\zeta_x + w\eta_y\zeta_y - \frac{2}{3}u\eta_x\zeta_z - \frac{2}{3}v\eta_y\zeta_z) \\ \quad + \kappa Pr^{-1}(\gamma-1)^{-1}(\eta_x\zeta_x + \eta_y\zeta_y + \eta_z\zeta_z)(a^2)_\zeta \end{bmatrix} \tag{A2}$$

$$\hat{S}^{\eta} = J^{-1}\begin{bmatrix} 0 \\ \mu[u_{\eta}(\frac{4}{3}\zeta_x\eta_x + \zeta_y\eta_y + \zeta_z\eta_z) + v_{\eta}(\zeta_y\eta_x - \frac{2}{3}\zeta_x\eta_y) + w_{\eta}(\zeta_z\eta_x - \frac{2}{3}\zeta_x\eta_z)] \\ \mu[u_{\eta}(\zeta_x\eta_y - \frac{2}{3}\zeta_y\eta_x) + v_{\eta}(\zeta_x\eta_x + \frac{4}{3}\zeta_y\eta_y + \zeta_z\eta_z) + w_{\eta}(\zeta_z\eta_y - \frac{2}{3}\zeta_y\eta_z)] \\ \mu[u_{\eta}(\zeta_x\eta_z - \frac{2}{3}\zeta_z\eta_x) + v_{\eta}(\zeta_y\eta_z - \frac{2}{3}\zeta_z\eta_y) + w_{\eta}(\zeta_x\eta_x + \zeta_y\eta_y + \frac{4}{3}\zeta_z\eta_z)] \\ \mu u_{\eta}(\frac{4}{3}u\zeta_x\eta_x + v\zeta_x\eta_y + w\zeta_x\eta_z + u\zeta_y\eta_y + u\zeta_z\eta_z - \frac{2}{3}v\zeta_y\eta_x - \frac{2}{3}w\zeta_z\eta_x) \\ \quad + \mu v_{\eta}(\frac{4}{3}v\zeta_y\eta_y + u\zeta_y\eta_x + w\zeta_y\eta_z + v\zeta_x\eta_x + v\zeta_z\eta_z - \frac{2}{3}u\zeta_x\eta_y - \frac{2}{3}w\zeta_z\eta_y) \\ \quad + \mu w_{\eta}(\frac{4}{3}w\zeta_z\eta_z + w\zeta_x\eta_x + w\zeta_y\eta_y + u\zeta_z\eta_x + v\zeta_z\eta_y - \frac{2}{3}u\zeta_x\eta_z - \frac{2}{3}v\zeta_y\eta_z) \\ \quad + \kappa Pr^{-1}(\gamma-1)^{-1}(\zeta_x\eta_x + \zeta_y\eta_y + \zeta_z\eta_z)(a^2)_{\eta} \end{bmatrix}, \tag{A3}$$

$$\hat{S}^{\zeta} = J^{-1}\begin{bmatrix} 0 \\ \frac{1}{3}\mu\zeta_x(\zeta_x u_{\zeta} + \zeta_y v_{\zeta} + \zeta_z w_{\zeta}) + \mu(\zeta_x^2 + \zeta_y^2 + \zeta_z^2)\, u_{\zeta} \\ \frac{1}{3}\mu\zeta_y(\zeta_x u_{\zeta} + \zeta_y v_{\zeta} + \zeta_z w_{\zeta}) + \mu(\zeta_x^2 + \zeta_y^2 + \zeta_z^2)\, v_{\zeta} \\ \frac{1}{3}\mu\zeta_z(\zeta_x u_{\xi} + \zeta_y v_{\zeta} + \zeta_z w_{\zeta}) + \mu(\zeta_x^2 + \zeta_y^2 + \zeta_z^2)\, w_{\zeta} \\ \{(\zeta_x^2 + \zeta_y^2 + \zeta_z^2)[\mu(uu_{\zeta} + vv_{\zeta} + ww_{\zeta}) + \kappa Pr^{-1}(\gamma-1)^{-1}(a^2)_{\zeta}] \\ \quad + \frac{1}{3}\mu(\zeta_x u + \zeta_y v + \zeta_z w)(\zeta_x u_{\zeta} + \zeta_y v_{\zeta} + \zeta_z w_{\zeta})\} \end{bmatrix}, \tag{A4}$$

REFERENCES

1. L. B. SCHIFF AND W. B. STUREK, "Numerical Simulation of Steady Supersonic Flow Over an Ogive-Cylinder-Boattail Body," AIAA 18th Aerospace Sciences Meeting, Pasadena, CA, January 14–16, 1980.
2. L. B. SCHIFF AND J. L. STEGER, *AIAA J.* **18**, 1421 (1980).
3. R. P. REKLIS AND W. B. STUREK, "Surface Pressure Measurements on Slender Bodies at Angle of Attack in Supersonic Flow," ARBRL-MR-02876, November 1978 (unpublished).
4. L. D. KAYSER AND W. B. STUREK, "Experimental Measurements in the Turbulent Boundary Layer of a Yawed, Spinning, Ogive-Cylinder Body of Revolution at Mach 3.0, Part II, Data Tabulation," ARBRL-MR-02813, March 1978 (unpublished).
5. L. D. KAYSER AND W. B. STUREK, "Turbulent Boundary Layer Measurements on the Boattail Section of a Yawed, Spinning Projectile Shape at Mach 3.0," ARBRL-MR-02880, November 1978 (unpublished).
6. R. M. BEAM AND R. F. WARMING, *AIAA J.* **16**, 393 (1978).
7. L. B. SCHIFF AND J. L. STEGER, "Numerical Simulation of Steady Supersonic Viscous Flow," NASA TP-1749, May 1981 (unpublished).
8. S. BOERSEN, "Reynolds Number Effects on Pressure and Normal Force Distributions Along Conically Pointed Circular Cylinder at Mach Number of 2.3," NLR TR 75124U, September, 1975 (unpublished).
9. M. TOBAK AND D. J. PEAKE, *Ann. Rev. Fluid Mech.* **14**, 61 (1982).
10. B. S. BALDWIN AND H. LOMAX, "Thin Layer Approximation and Algebraic Model for Separated Turbulent Flows," AIAA 16th Aerospace Sciences Meeting, Huntsville, AL, January 16–18, 1978.

11. T. CEBECI, "Calculation of Compressible Turbulent Boundary Layers with Heat and Mass Transfer," AIAA 3rd Fluid and Plasma Dynamics Conference, Los Angeles, CA, June 29–July 1, 1970.
12. D. DEGANI AND J. L. STEGER, *AIAA J.* **21**, 1604 (1983).
13. C. J. NIETUBICZ, U. S. Army Ballistic Research Lab., Aberdeen, MD, unpublished wind-tunnel data, private communication (1979).
14. W. J. RAINBIRD, *AIAA J.* **6**, 2410 (1968).
15. W. J. RAINBIRD, "The External Flow Field About Yawed Circular Cones," Hypersonic Boundary Layers and Flow Fields, AGARD CP-30, 1968 unpublished).
16. C. NEBBELING AND W. J. BANNINK, *J. Fluid Mech.* **87**, 475 (1978).
17. W. J. BANNINK AND C. NEBBELING, "Measurement of the Supersonic Flow Field Past a Slender Cone at High Angles of Attack," High Angle of Attack Aerodynamics, AGARD CP-247, 1978 (unpublished).